Quantitative Analysis of Near-Surface Seismological Complexity Based on the Generalized Lippmann–Schwinger Matrix Equation

by Bin Liu,[*] Li-Yun Fu,[†] Geng-Xin Yu, and Gao-Xiang Chen[‡]

Abstract   Near-surface complexity is characteristic of rugged topographies and strong volume heterogeneities, which significantly affects seismic data recorded at the free surface. An efficient method is presented here to quantitatively analyze the near-surface seismological complexity. We use a boundary–volume element numerical method to discretize the generalized Lippmann–Schwinger integral equation formulated in terms of volume scattering and boundary scattering. The integral equation technique provided sufficient accuracy to model rough topographies, large-scale structures, and volume heterogeneities in a straightforward and efficient manner. Rather than solving the resultant global matrix equation at a very high computational cost, certain characteristic parameters of the scattering amplitude matrix were estimated and used as indicators to assess the near-surface seismological complexity. Applications to numerous examples validated the method's applicability, reliability, and efficiency, whereby the resultant matrix characteristic parameters varied consistently with the near-surface complexity in geometric structures, volume heterogeneities, and computational frequencies.

Introduction

Near-surface complexity impacts ground-motion observations, seismic exploration, and near-surface geophysics. Site amplification of ground motions is strongly related to near-surface geometries and near-surface heterogeneities. Rugged topographies and general heterogeneities in near-surface sediments cause semirandom and semicoherent near-surface scattering of wavefields that challenge seismic acquisition design and seismic data denoising in seismic exploration. Numerical simulations of wave propagation have been used extensively to analyze near-surface seismological complexity; however, it is difficult to express this complexity directly from simulated wavefields. It is also difficult to integrate the deterministic and statistical descriptions of near-surface geometries directly into wave propagation. Few studies focused on near-surface seismological complexity by combining near-surface geometries, near-surface heterogeneities, and near-surface wavefields. The current study presents a method to efficiently combine waves and near-surface features for directly evaluating near-surface seismological complexity. The resulting near-surface complexity coefficient provides a reference for seismic acquisition design and seismic data denoising. It is expected that this method will be helpful for assessing site amplification of ground motion.

Near-surface complexity is strongly related to rugged topographies and volume heterogeneities in near-surface sediments, causing strong near-surface scatterings (volume scattering and boundary scattering). Bouchon *et al.* (1989, 1996) provide a comprehensive review of topographic effects on wave propagation, which mainly fall into two categories: (1) deterministic and (2) statistical descriptions for rough surface scattering. The former category (Bouchon, 1973; Hudson *et al.*, 1973; Sabina and Willis, 1975; Chen, 1990; Sánchez-Sesma and Campillo, 1991, 1993; Fu, 2003) is based on surface height and surface slope for a given topographic irregularity to investigate the effects of seismological complexity on the amplification of ground motion. The latter category (Fu *et al.*, 2002; Fu, 2005; Hu *et al.*, 2009) is based on random roughness in terms of wavenumber, surface root mean square height, surface correlation length, and propagation distance. These studies provide insights into the topographic effect on wave propagation but have difficulty directly expressing the near-surface seismological complexity from a simulated wavefield or a mathematic description of near-surface geometries. Therefore, a straightforward and efficient index of seismological complexity to investigate near-surface effects on ground-motion amplification is presented, and an evaluation criterion can be extracted directly from near-surface matrix equations as a combination of

---

*Also at University of Chinese Academy of Sciences, Beijing, China.

†Also at Key Laboratory of the Earth's Deep Interior, Institute of Geology and Geophysics, Chinese Academy of Sciences, Beijing, China.

‡Also at Zhejiang Provincial Institute of Communication, Planning, Design and Research, Zhejiang, China.

near-surface geometries, near-surface heterogeneities, and near-surface wavefields.

Modeling near-surface sediments challenges numerical methods because of rugged topographies, strong volume heterogeneities, and traction-free condition. The finite-difference and pseudospectral methods are flexible enough for modeling generally heterogeneous media. However, these methods use implicit boundary conditions and the complex gridding discretization to irregular boundaries, resulting in limited accuracy for modeling boundary waves. Targeted at wave propagation in complex near-surface media, numerical modeling techniques with explicit use of boundary conditions have been studied extensively. By incorporating the boundary integral representation into the Lippmann–Schwinger integral equation, the resultant generalized Lippmann–Schwinger integral equation (GLSIE; Fu, 2002) is formulated in terms of volume scattering and boundary scattering and describes the combined effects of rugged topographies, sedimentary structures, and volume heterogeneities in a straightforward and efficient manner.

The current study applied a boundary–volume element numerical method (Fu and Bouchon, 2004) to the boundary–volume integral equation. The resultant global coefficient matrix was sparse and narrowbanded depending on the near-surface structure. This integral equation technique provided sufficient accuracy to model complex near-surface media through the geometrically accurate description of rugged topographies, the explicit use of boundary conditions, and the ability to deal with volume heterogeneities. Rather than solving the global matrix equation using costly computing time, the matrix analysis technique was used to extract cer-
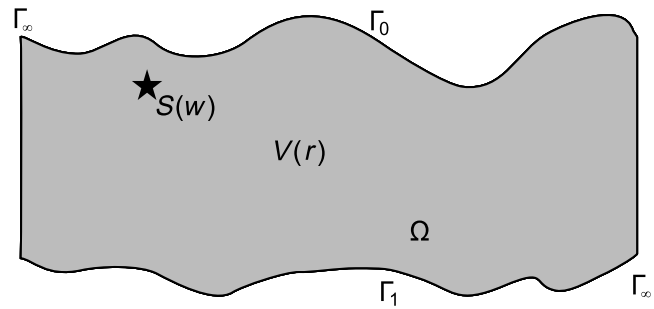

Figure 1. Geometry of a scattering medium in homogeneous free space.

tain characteristic parameters from the scattering amplitude matrix, leading to an indicator for assessing near-surface seismological complexity. This quantitative analysis method was applied to numerous examples to validate the method's applicability, reliability, and efficiency.

Methodology

Wave propagation in the near-surface region is characterized by volume heterogeneities and rugged topographies, which can be described by a GLSIE. The problem studied is illustrated in Figure 1. The formation Ω is bounded by a heterogeneous structure that contains a rough uppermost boundary Γ_0, an irregular interface Γ_1, and artificial boundaries Γ_∞. These boundaries form a closed surface $\Gamma = \Gamma_0 + \Gamma_1 + \Gamma_\infty$, and the solution domain of the problem is defined as $\bar{\Omega} = \Omega + \Gamma$. Supposing the source point is
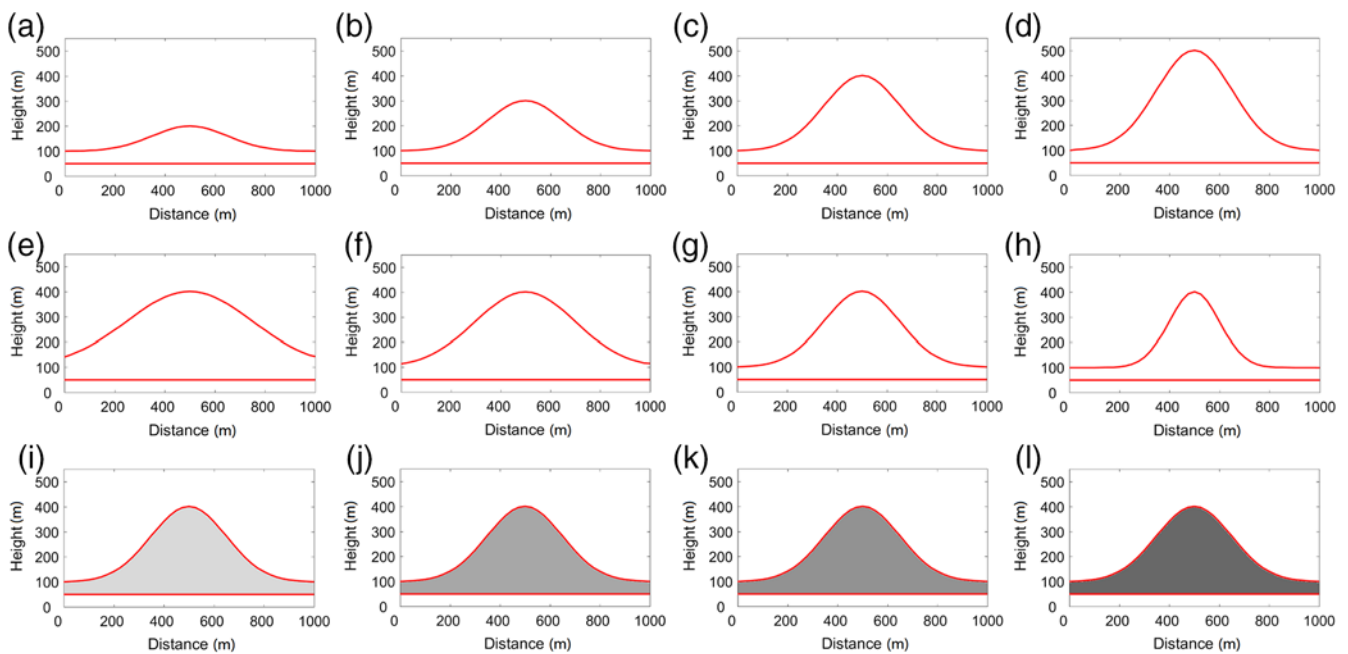

Figure 2. Models of different peak heights, topographic slopes, and velocity perturbations (a–d: 100, 200, 300, and 400 m peak height; e–h: 26.57°, 30.96°, 36.87°, and 45.00° slope angle; i–l: 15%, 20%, 25%, and 30% velocity perturbation). The color version of this figure is available only in the electronic edition.
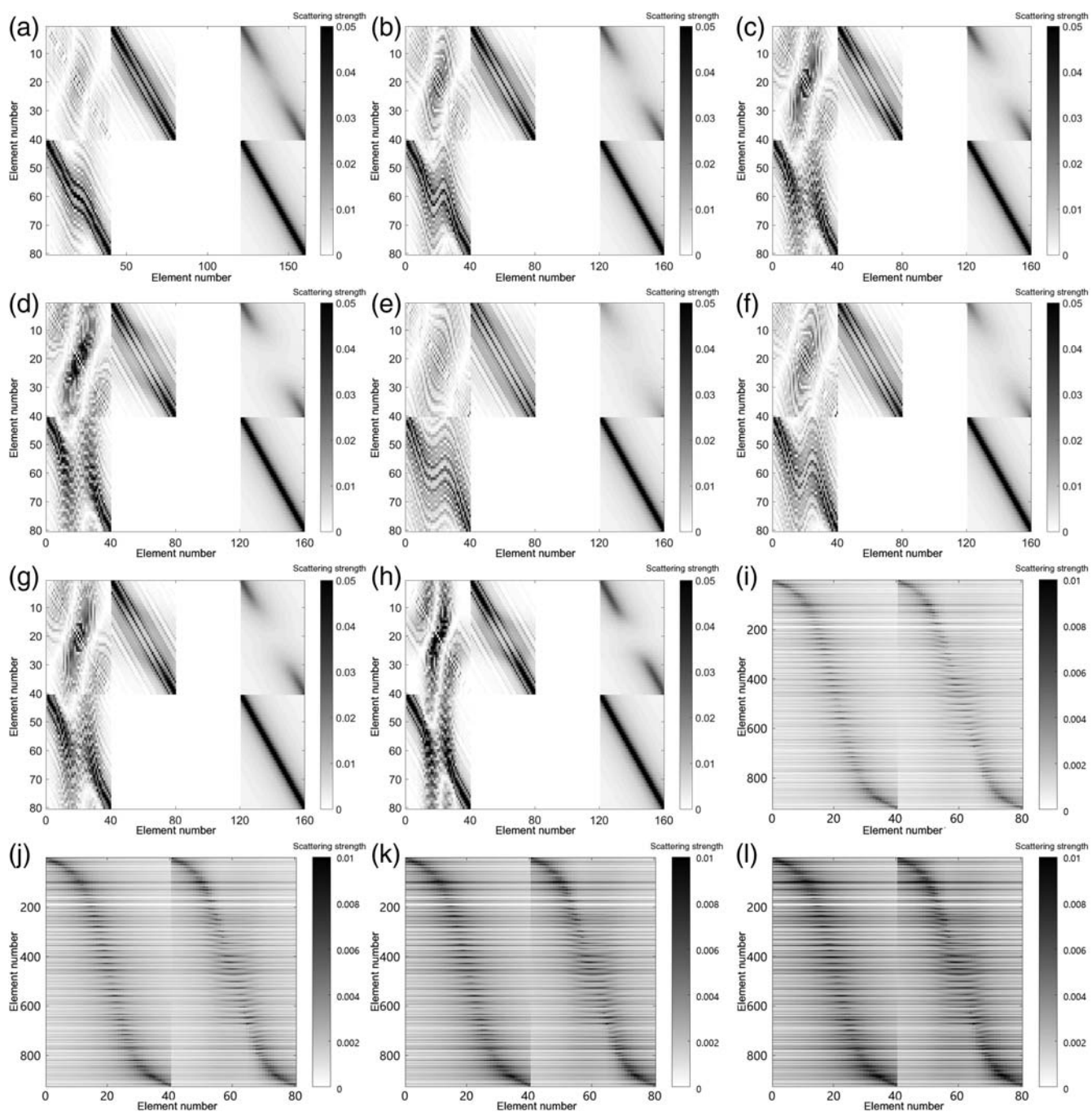
Figure 3. Corresponding matrices of different peak heights, topographic slopes, and velocity perturbations (a–d: 100, 200, 300, and 400 m peak height; e–h: 26.57°, 30.96°, 36.87°, and 45.00° slope angle; i–l: 15%, 20%, 25%, and 30% velocity perturbation).
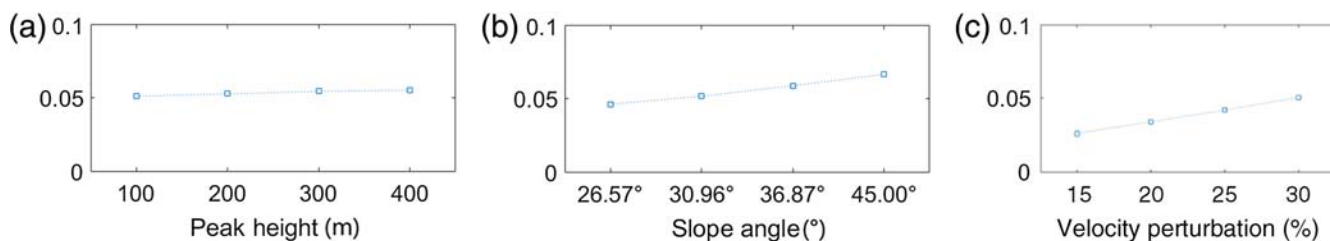

Figure 4. Scalar complexity coefficients of models in Figure 2. The color version of this figure is available only in the electronic edition.
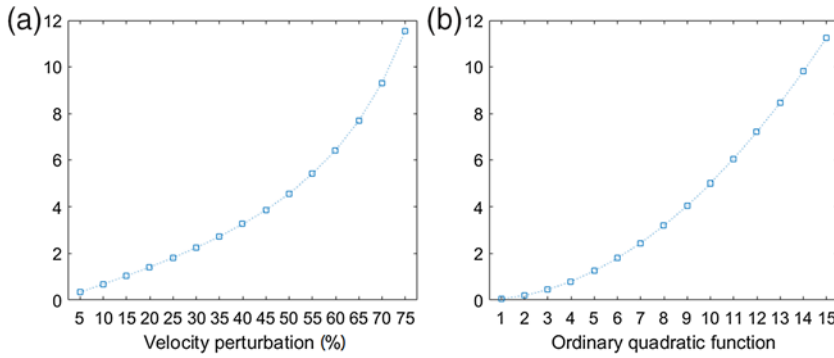
Figure 5. Variation of complexity coefficient and normal quadratic function. The color version of this figure is available only in the electronic edition.
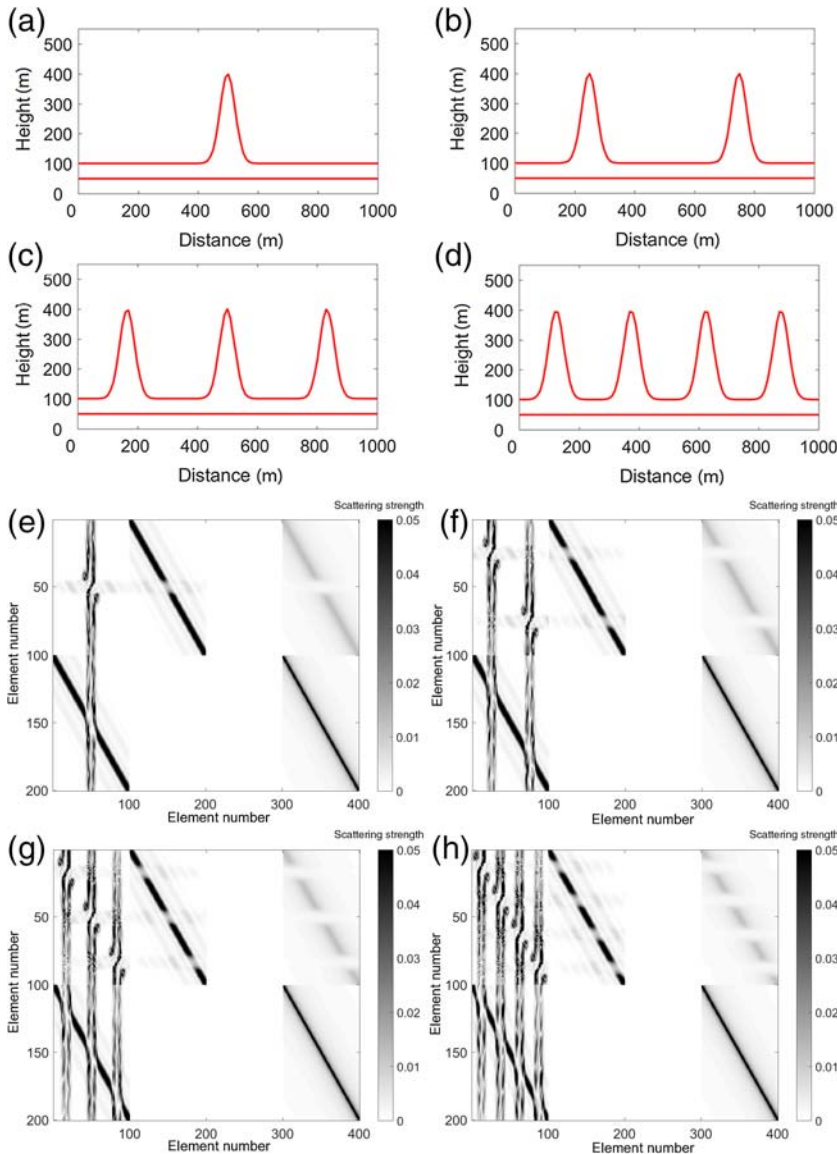

Figure 6. Models of different peak numbers and corresponding scattering amplitude matrices. The color version of this figure is available only in the electronic edition.

located at $\mathbf{r}_0$, the source term can be expressed as $S(\mathbf{r}, \omega) = S(\omega)\delta(\mathbf{r} - \mathbf{r}_0)$, in which $S(\omega)$ is the source spectrum and $\delta(\mathbf{r} - \mathbf{r}_0)$ is the delta distribution. Steady-state scalar wave propagation in this medium satisfies the scalar Helmholtz wave equation in the frequency domain

$$\nabla^2 u(\mathbf{r}) + k^2 u(\mathbf{r}) = -s(\mathbf{r}, \omega), \qquad (1)$$

in which ω is the angular frequency, $k = \omega/v(\mathbf{r})$ is the wavenumber, and $v(\mathbf{r})$ is the velocity distribution in the background with a constant velocity v_0.

The seismic response $u(\mathbf{r})$ also satisfies the following boundary conditions: (1) the traction-free condition on the free surface: $\frac{\partial u(\mathbf{r})}{\partial n} = 0$ at $\mathbf{r} \in \Gamma_0$; (2) the continuities of displacement and traction at the interface, $u_i^-(\mathbf{r}) = u_i^+(\mathbf{r})$, and $\frac{\partial u_i^-(\mathbf{r})}{\partial n} = \frac{\partial u_i^+(\mathbf{r})}{\partial n}$, at $\mathbf{r} \in \Gamma_i$, in which "$-$" denotes the top side of toward Γ_i and "$+$" denotes the underside of toward Γ_i; (3) the radiation boundary condition imposed on the far-field behavior at infinity, that is, $\lim_{|\mathbf{r}| \to \infty} u(\mathbf{r}) = 0$ and $\lim_{|\mathbf{r}| \to \infty} \frac{\partial u(\mathbf{r})}{\partial r} = 0$.

The total seismic response $u(\mathbf{r})$ at location $\mathbf{r} \in \Omega$ is composed of

$$u(\mathbf{r}) = u^0(\mathbf{r}) + u^1(\mathbf{r}) + u^2(\mathbf{r}), \qquad (2)$$

in which $u^0(\mathbf{r})$ is the incident field in the background medium, which can be represented as

$$u^0(\mathbf{r}) = \int_\Omega s(\mathbf{r}', \omega) G(\mathbf{r}, \mathbf{r}') d\mathbf{r}'$$
$$= S(\omega) G(\mathbf{r}, \mathbf{r}_0) \qquad (3)$$

and $u^1(\mathbf{r})$ is the scattered field by the irregular boundary and satisfies the boundary integral equation

$$u^1(\mathbf{r}) = \int_\Gamma \left[G(\mathbf{r}, \mathbf{r}') \frac{\partial u(\mathbf{r}')}{\partial n} - u(\mathbf{r}') \frac{\partial G(\mathbf{r}, \mathbf{r}')}{\partial n} \right] d\mathbf{r}', \qquad (4)$$

in which $G(\mathbf{r}, \mathbf{r}')$ is Green's function, which can be represented as $G(\mathbf{r}, \mathbf{r}') = \frac{1}{4} i H_0^{(1)}(k_0 |\mathbf{r} - \mathbf{r}'|)$ in 2D problems. Similarly, $\frac{\partial G(\mathbf{r}, \mathbf{r}')}{\partial n} = -\frac{1}{4} i H_1^{(1)}(k_0 |\mathbf{r} - \mathbf{r}'|) \frac{\partial k_0 |\mathbf{r} - \mathbf{r}'|}{\partial n}$ is the normal derivative of Green's function.

$u^2(\mathbf{r})$ is the field scattered by volume heterogeneities within Ω and satisfies the
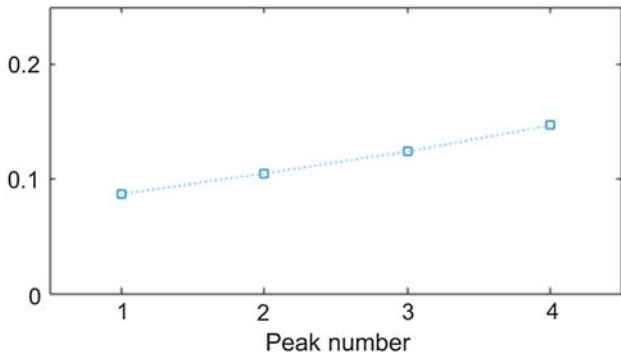
Figure 7. Scalar complexity coefficients of models in Figure 6. The color version of this figure is available only in the electronic edition.
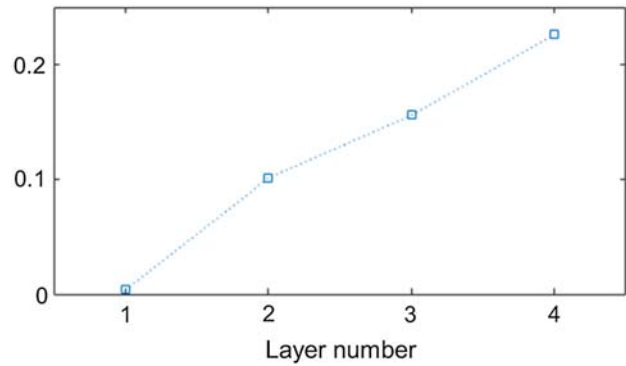

Figure 9. Scalar complexity coefficients of models in Figure 8. The color version of this figure is available only in the electronic edition.

Lippmann–Schwinger integral equation

$$u^2(\mathbf{r}) = k_0^2 \int_\Omega O(\mathbf{r}')u(\mathbf{r}')G(\mathbf{r}, \mathbf{r}')d\mathbf{r}',$$

(5)

in which $k_0 = \omega/v_0$ is the background wavenumber and $O(\mathbf{r})$ is the perturbed velocity function defined as $O(\mathbf{r}) = \frac{v_0^2}{v^2(\mathbf{r})} - 1$. For homogeneous media, $O(\mathbf{r}) = 0$ and $u^2(\mathbf{r}) = 0$.

Substituting equations (3)–(5) into equation (2), the GLSIE was obtained:

$$\int_\Gamma \left[G(\mathbf{r}, \mathbf{r}')\frac{\partial u(\mathbf{r}')}{\partial n} - u(\mathbf{r}')\frac{\partial G(\mathbf{r}, \mathbf{r}')}{\partial n} \right]d\mathbf{r}'$$

$$+ k_0^2 \int_\Omega O(\mathbf{r}')u(\mathbf{r}')G(\mathbf{r}, \mathbf{r}')d\mathbf{r}'$$

$$+ S(\omega)G(\mathbf{r}, \mathbf{r}_0)$$

$$= \begin{cases} u(\mathbf{r}) & \mathbf{r} \in \Omega \\ C(\mathbf{r})u(\mathbf{r}) & \mathbf{r} \in \Gamma, \\ 0 & \mathbf{r} \notin \bar{\Omega} \end{cases}$$

(6)

in which the coefficient $C(\mathbf{r})$ depends on the geometry at $\mathbf{r}$ for all $\mathbf{r}' \in \bar{\Omega}$. For smooth boundaries, $C(\mathbf{r}) = 0.5$.

The discretization of equation (6) can be done by the collocation method. Boundary Γ is divided into L boundary elements denoted by $\Gamma_e(e = 1, 2, ..., L)$, whereas domain Ω is divided into M elements, denoted by $\Omega_e(e = 1, 2, ..., M)$ resulting in a total of N nodes. Using the linear interpolation shape function Φ in an element between the nodes I_1 and I_2, the variables are approximated by the linear combination of their node values over the element, for example
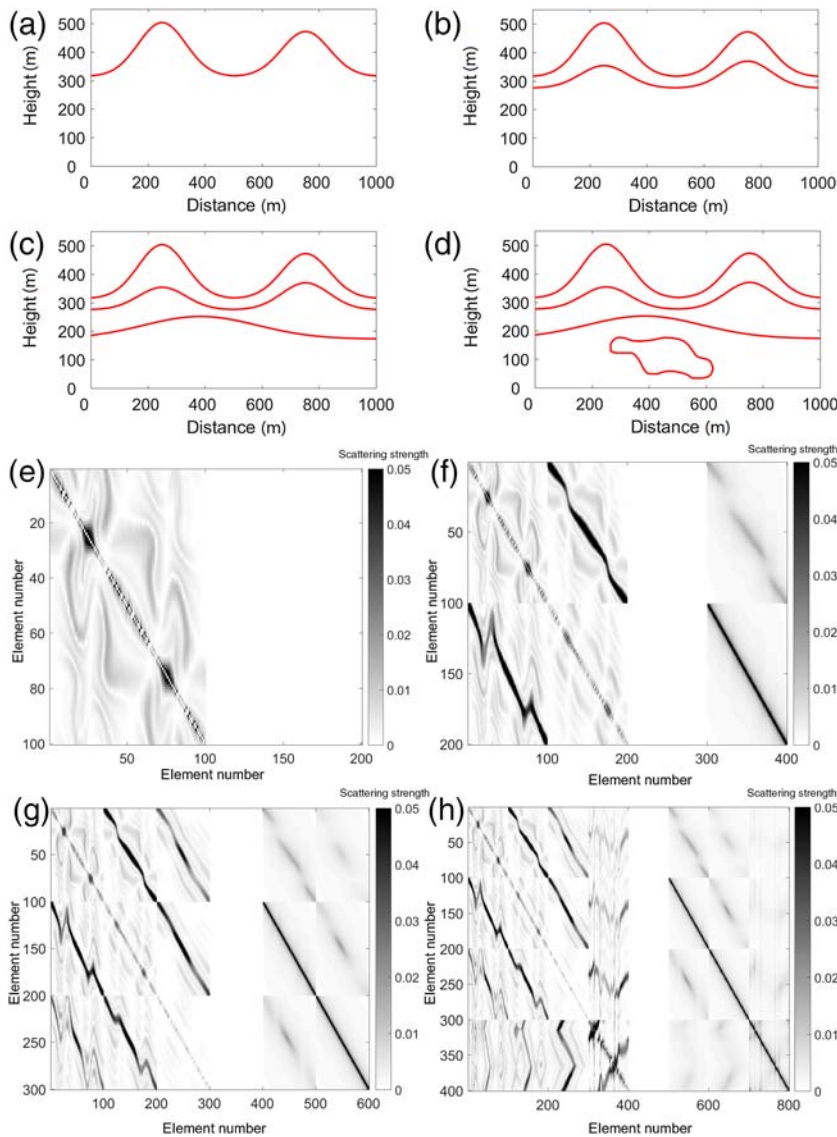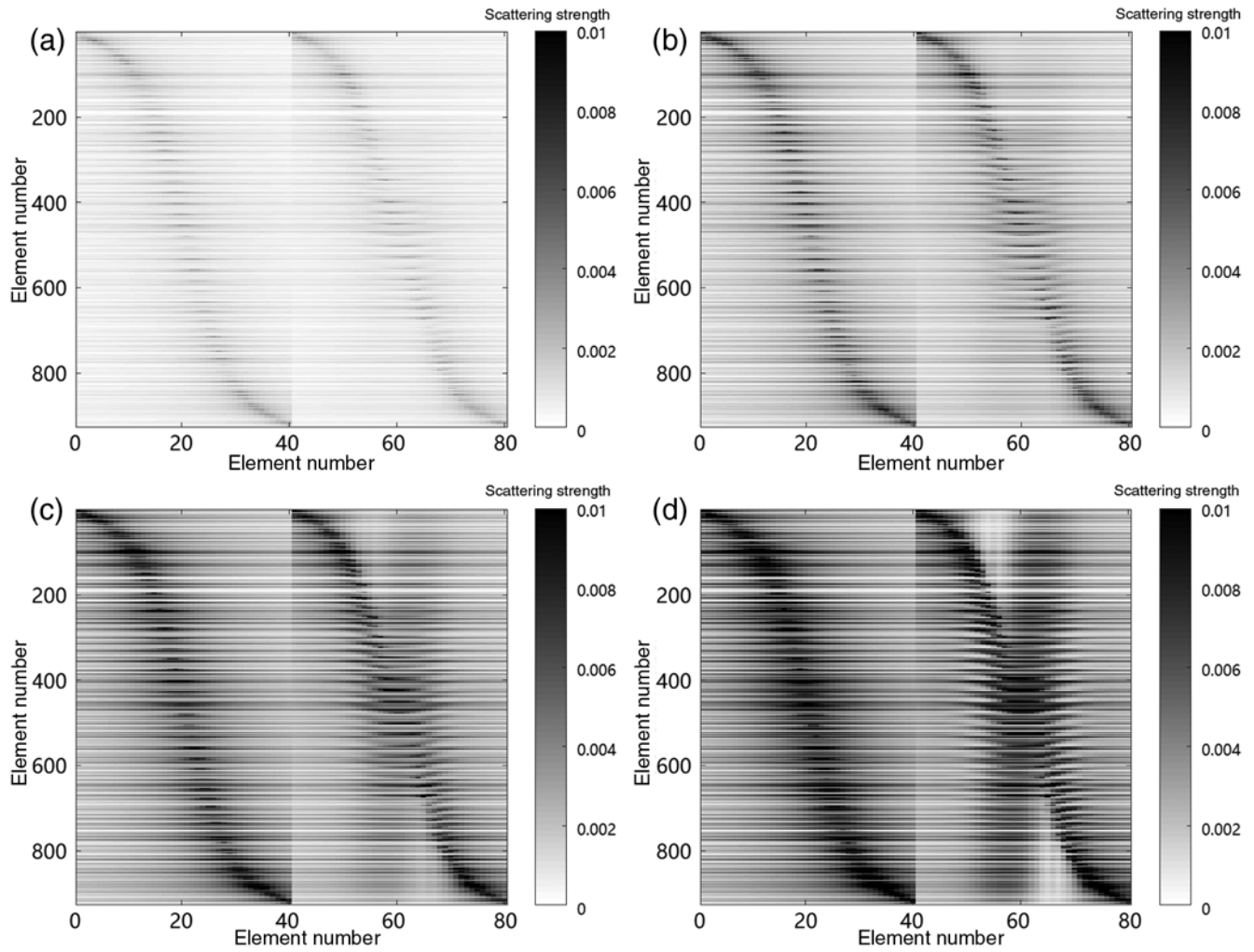

Figure 8. Mutilayer models and corresponding scattering amplitude matrices. The color version of this figure is available only in the electronic edition.

Figure 10. Scattering amplitude matrices from Figure 2j with frequencies of 15, 30, 45, and 65 Hz.

$$u(\xi) = \sum_{l=I_1}^{I_2} u(\mathbf{r}_l)\Phi_l(\xi), \qquad (7)$$

in which ξ denotes the local coordinates of an element. Then, the integral equation (6) was rewritten in operator form
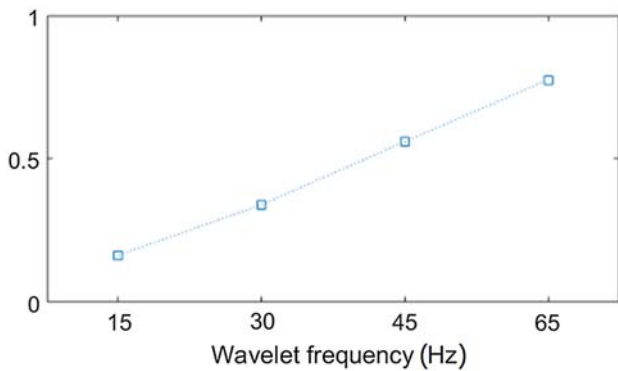

Figure 11. Scalar complexity coefficients of different wave frequency. The color version of this figure is available only in the electronic edition.

$$Hu^{(1)}(\mathbf{r}_i) - Gt(\mathbf{r}_i) = Ku^{(2)}(\mathbf{r}_i) + f(\mathbf{r}_i),$$
$$i = 1, 2, \ldots, N, \qquad (8)$$

in which $u^{(1)}$ is the seismic response at Γ, t is the normal derivative of $u^{(1)}$ with respect to the outward normal to Γ, $u^{(2)}$ is the seismic response in Ω, f is the incident wavefield, H and G are the boundary integral operators, and K is the perturbation-domain integral operator. The integrals in equation (6) can be computed over each element as
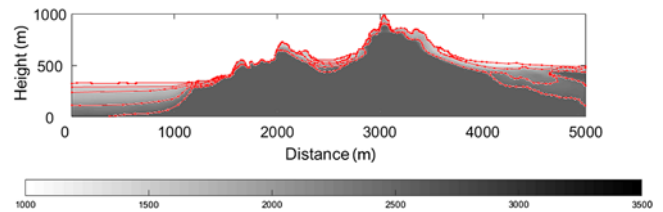

Figure 12. Actual near-surface velocity structure of a certain area. The color version of this figure is available only in the electronic edition.
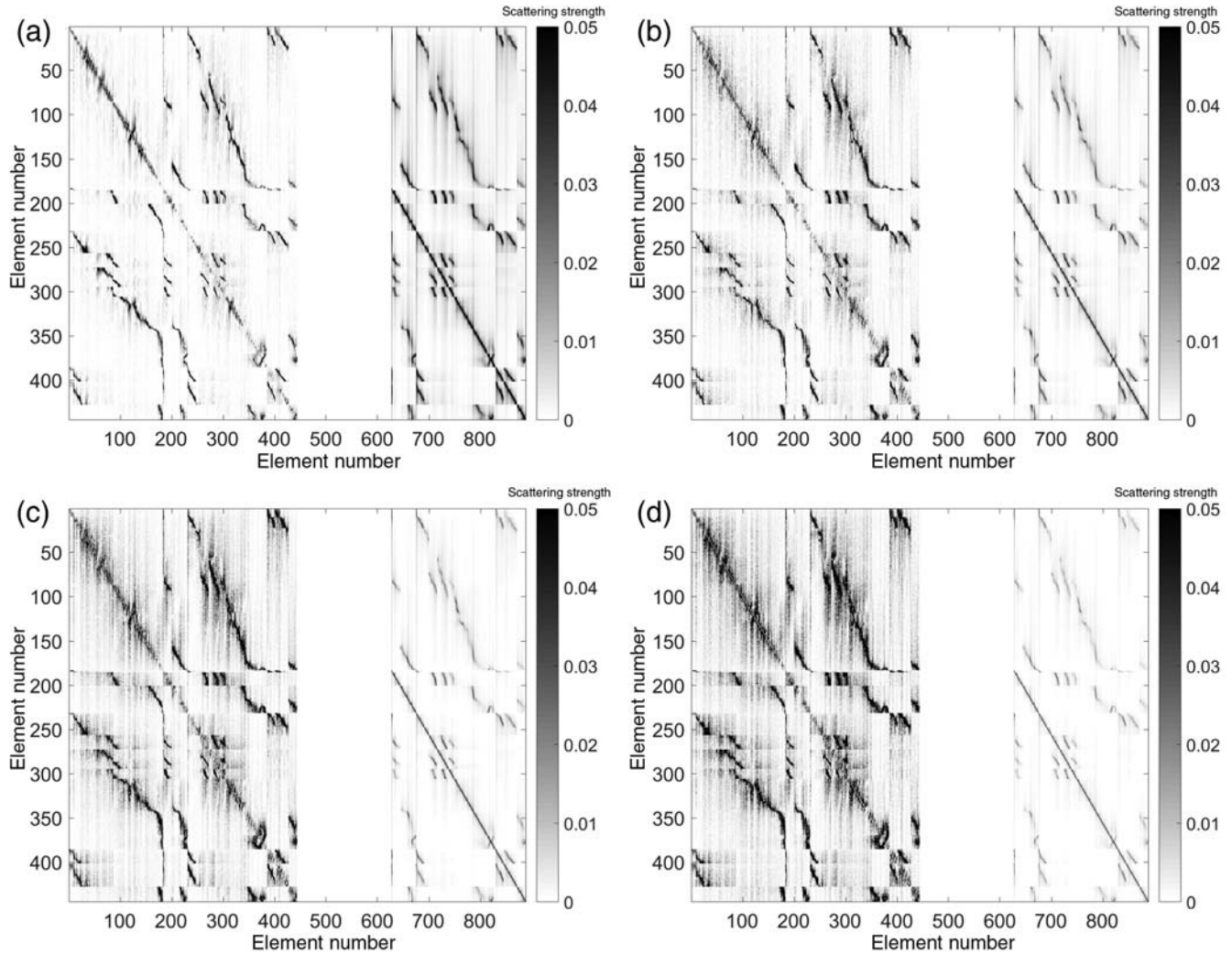
Figure 13.   Scattering amplitude matrices from Figure 12 when the frequency is 15, 30, 45, and 65 Hz.

$$H_{ij} = \sum_{e=1}^{L} \sum_{l=I_1}^{I_2} \left[\int_{\Gamma_e} \frac{\partial}{\partial n} G(\mathbf{r}_i, \mathbf{r}'(\xi)) \Phi_l(\xi) d\mathbf{r}'(\xi) \right] + C(\mathbf{r}_i)\delta_{ij},$$

$$(9)$$

$$G_{ij} = \sum_{e=1}^{L} \sum_{l=I_1}^{I_2} \left[\int_{\Gamma_e} G(\mathbf{r}_i, \mathbf{r}'(\xi)) \Phi_l(\xi) d\mathbf{r}'(\xi) \right], \qquad (10)$$

$$K_{ij} = \sum_{e=1}^{M} \sum_{l=I_1}^{I_2} \left[\int_{\Omega_e} k_0^2 O(\mathbf{r}'(\xi)) G(\mathbf{r}_i, \mathbf{r}'(\xi)) \Phi_l(\xi) d\mathbf{r}'(\xi) \right] - \delta_{ij},$$

$$(11)$$

in which δ_{ij} is the Kronecker delta function, and the Gaussian integration algorithm is used to numerically evaluate these integrals.

Herein, the resultant H, G, and K matrices were used to quantitatively analyze near-surface seismological complexity. The G matrix (i.e., the fundamental solution) characterized the effect on wavefield associated with propagation distances between arbitrary boundary elements. The H matrix (i.e., the normal derivative of the fundamental solution) contained the information of topographic roughness in terms of the relative position of two boundary elements. The K matrix featured the volume scattering by near-surface heterogeneities. Therefore, these matrices can reflect near-surface seismological complexity in some respect.

As a tentative attempt to characterize the global coefficient matrix, a characteristic index "comp", was defined to quantitatively analyze near-surface seismological complexity. Let comp = comp1 + comp2, in which comp1 represents the boundary scattering effect, and comp2 indicates the scattering effect of volume heterogeneities, then comp can be expressed as the combination of two scattering effects. Because of large differences between H and G in the matrix calculation, normalization of H, G, and K was required here. The feature scaling method is used here to do the normalization process, that is

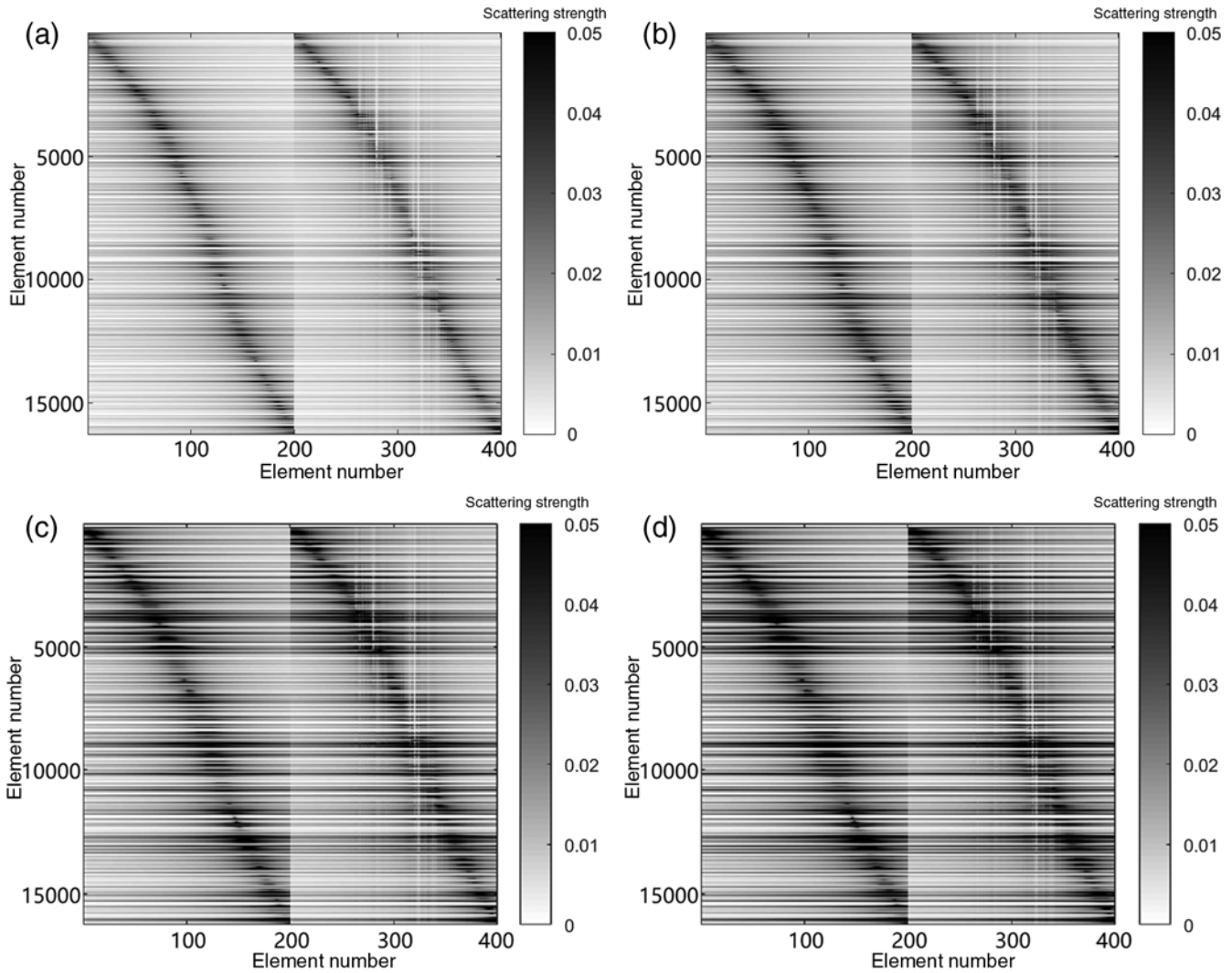$$X' = \frac{X - X_{\min}}{X_{\max} - X_{\min}}, \qquad (12)$$

Figure 14. Scattering amplitude matrices from Figure 12 with velocity perturbations of 15%, 20%, 25%, and 30%.

in which X' represents the element of the normalized matrix, X represents the element of the original matrix, and $X_{\min}$ and $X_{\max}$ represent the minimum and maximum elements in the original matrix.

Let

$$
\begin{aligned}
\text{comp1} &= \frac{\sum_{i=1}^{L}\sum_{j=1}^{L}\bar{H}}{L} + \frac{\sum_{i=1}^{L}\sum_{j=1}^{L}\bar{G}}{L} \\
&= \frac{\sum_{i=1}^{2L}\sum_{j=1}^{L}\bar{A}}{L},
\end{aligned} \tag{13}
$$

in which $\bar{A} = [\bar{H}, \bar{G}]$, $\bar{H}$ and $\bar{G}$ represent the normalized matrices of H and G, and L is the number of the boundary element. For a surface seismic survey, matrix G can be removed in the equation considering the free surface condition.

Similarly, comp2 is defined as

$$
\text{comp2} = \frac{\sum_{i=1}^{L}\sum_{j=1}^{M}\bar{K}}{L}, \tag{14}
$$

in which $\bar{K}$ represents the normalized matrix of K, and M is the number of the volume element.

This produced

$$
\text{comp} = \frac{\sum_{i=1}^{2L}\sum_{j=1}^{L}\bar{A}}{L} + \frac{\sum_{i=1}^{L}\sum_{j=1}^{M}\bar{K}}{L}. \tag{15}
$$

In this method, the characteristic parameter comp (i.e., the ratio of the summation of all matrix elements and its dimensions) can be estimated to quantitatively analyze near-surface seismological complexity, with great savings of computing cost and memory.

Numerical Examples

In this section, the results of validation of the quantitative analysis by numerous examples are presented that demonstrate its applicability, reliability, and efficiency. First, the method was used to analyze the scattering effects of Gaussian topographies with different heights, slopes (given by the local surface tangent), velocity perturbations, and peaks. This method was then applied to several multilayer models with irregular interfaces. For convenience of comparison, the resultant matrix characteristic parameters were calculated using normalization,
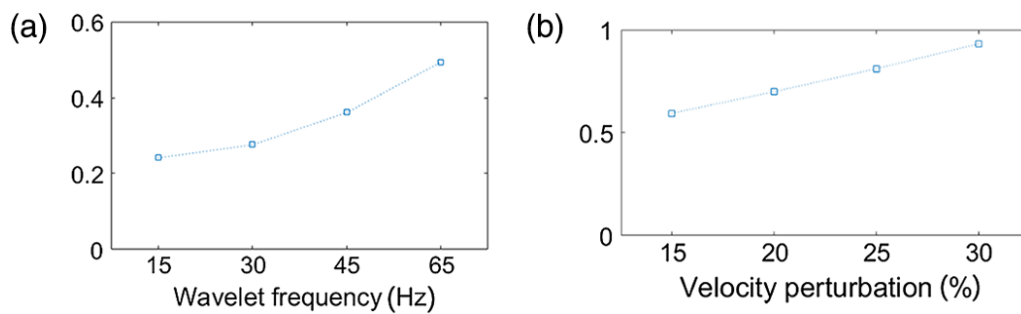
Figure 15.   Scalar complexity coefficients for different wave frequencies in practical tests. The color version of this figure is available only in the electronic edition.
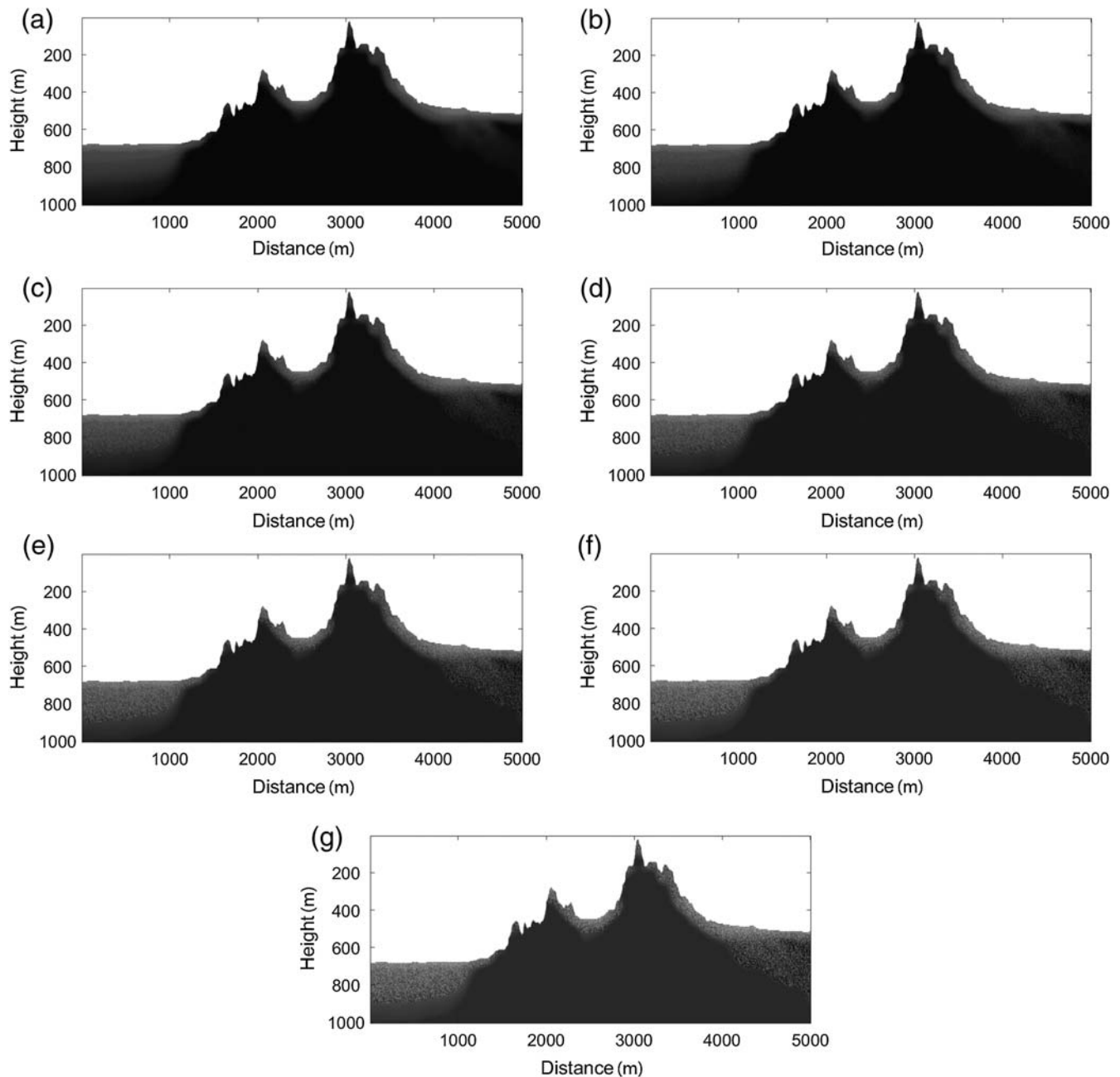

Figure 16.   Velocity field of different situations (a: homogeneous; b–g: 5%, 10%, 15%, 20%, 25%, and 30% random velocity perturbations).
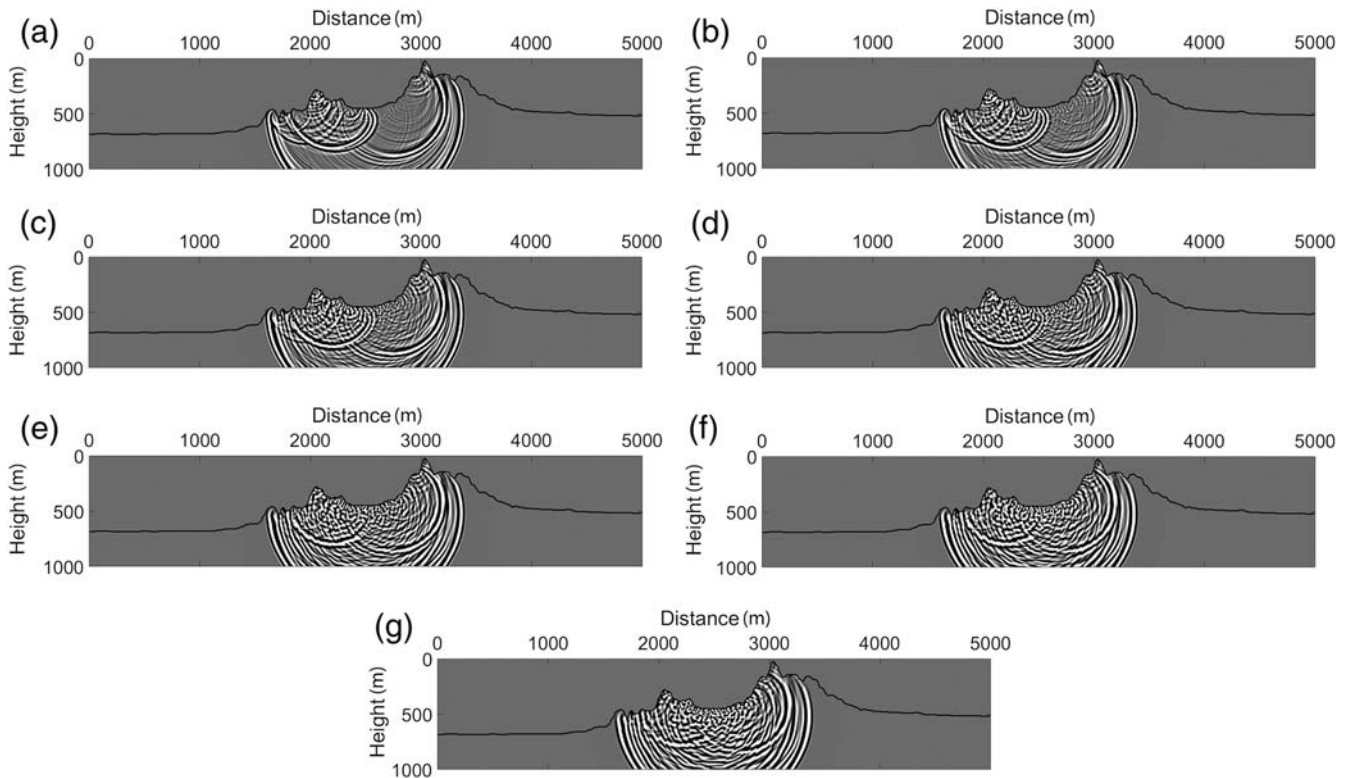
Figure 17. Wavefield snapshots at 1.0 s moment of the areas above (a: homogeneous; b–g: 5%, 10%, 15%, 20%, 25%, and 30% random velocity perturbations).

resulting values between 0 and 1. The background velocity was 3000 m/s and the computational frequency was 30 Hz for these examples.

Gaussian Topographies with Different Heights and Slopes

Geometrical heterogeneities of surface topography can be characterized by different statistical parameters. The models in the current study were designed to illustrate the scattering effects of surface height, slope angle, and volume heterogeneities. Figure 2a–d shows Gaussian topographies with different heights of 100, 200, 300, and 400 m, respectively. In Figure 2e–h, the Gaussian topographies change with the same height of 300 m and different slopes angles of 26.57°, 30.96°, 36.87°, and 45.00°. Figure 2i–l indicates that the near-surface media are heterogeneous with velocity perturbations of 15%, 20%, 25%, and 30%, respectively. For example, the 20% perturbation of the 3000 m/s reference velocity indicated that the velocities would change randomly from 2400 to 3600 m/s. In addition, for the matrix $\bar{H}$, the horizontal interface has no scattering effect to itself due to $\frac{\partial G(\mathbf{r}, \mathbf{r}')}{\partial n} = 0$ in the horizontal case. Also, for the matrix $\bar{G}$, the peak has zero-scattering effect to itself and to the horizontal interface because of the traction-free condition: $\frac{\partial u(\mathbf{r})}{\partial n} = 0$ at $\mathbf{r} \in \Gamma_0$, so the corresponding element in the matrix $\bar{A}$ is zero.

Figure 3 shows the corresponding scattering amplitude matrices for the different models in Figure 2. It can be seen from Figure 3 that the scattering amplitude matrices of the more complicated models (i.e., with greater height, steeper slope, or stronger velocity perturbation) had a higher grayscale. The higher the grayscale, the stronger the scattering strength.

The results shown in Figure 4 indicate that the characteristic parameter gradually became larger with increasing surface heights, slope angles, and velocity perturbations, consistent with previous studies in ground-motion amplification. It appears that velocity perturbations had a clearer impact on the scattering effect than the other two parameters (i.e., surface height and slope angle). Additionally, as the perturbation increased from 5% to 75% (Fig. 5), the trend of the scalar coefficient was more like a quadratic function rather than a linear function as shown in Figure 4c.

Gaussian Topographies with Different Peak Number

Models with different peak number were also calculated as shown in Figure 6a–d. The comparisons demonstrated that the high value area became denser and that the grayscale became higher with the increased peak number (Fig. 6e–h). The results in Figure 7 also showed that the multipeak model generated a stronger scattering effect than the single-peak model.

Multilayered Models

To show the effect of boundary scattering from rough topography, the presented method was applied to the
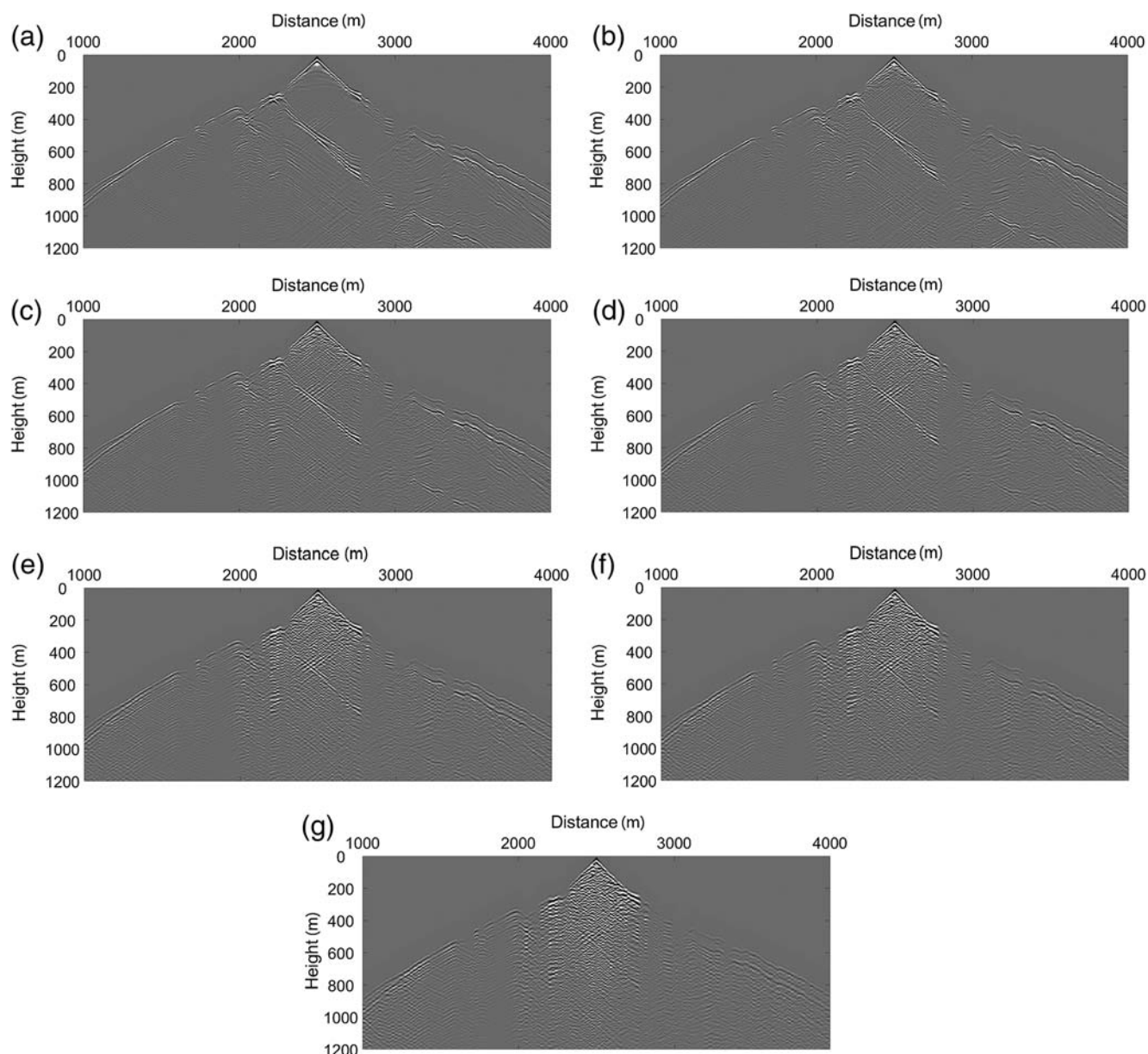
Figure 18. Single shot records of the areas above (a: homogeneous; b–g: 5%, 10%, 15%, 20%, 25%, and 30% random velocity perturbations).

multilayered models (Fig. 8). The scattering amplitude matrix had a larger grayscale area with the increasing interfaces of the multilayered models. Figure 9 shows that the characteristic parameter varied consistently with the complexity of the multilayered models.

Models with Different Computational Frequency

The above examples were calculated using the same frequency. The model shown in Figure 2j was simulated with computational frequencies of 15, 30, 45, and 65 Hz, respectively, to assess the influence of computational frequency. Here, the random velocity perturbation was 20%. It can be seen in Figure 10 that the grayscale became higher with

increasing frequency. The result shown in Figure 11 also demonstrated the same trend.

Practical Test

To further demonstrate the applicability of this method, the modeling was extended to a practical near-surface structure as shown in Figure 12. Modeling such near-surface complex media challenges numerical techniques because of rugged topographies, strong heterogeneities, and low near-surface velocities. The examples given in this section illustrate the usefulness of the method for assessing practical near-surface complexity.

Figure 13 shows the corresponding scattering amplitude matrices with different frequencies of 15, 30, 45, and 65 Hz for homogeneous near-surface media. Figure 14 indicates the corresponding scattering matrices with random velocity perturbation of 15%, 20%, 25%, and 30% and a frequency of 30 Hz for the heterogeneous near-surface media. The matrix values of the latter were higher than those of the former.

The comparisons in Figure 15 also verified the above analysis. It appears that for such practical cases, the volume scattering may be the dominant factor of scattering noise.

To make the comparison clearer, synthetic seismograms of the model were calculated by the boundary–volume element numerical method (Fu and Bouchon, 2004) with a 0–65 Hz frequency range for random velocity perturbations of 0%, 5%, 10%, 15%, 20%, 25%, and 30%, respectively, in the near-surface media. The corresponding velocity models are shown in Figure 16. The dimension of the model were 5000 m horizontally and 1000 m vertically. The source was a Ricker wavelet with a main frequency of 30 Hz, located at 2500 m in the abscissa of the free surface. The horizontal and vertical grid spacing was 5 m, and the time sampling interval was 0.001 s and a sampling time of 1.2 s.

Figure 17a shows strong boundary scattering caused by the rugged surface for the homogeneous media. With increasing velocity perturbation, volume scattering became gradually stronger (Fig. 17). These strong diffuse scatterings break up wavefronts, which become strong scattering noise for exploration seismology. The results in Figure 18 also demonstrate the combined effects of both rough topography and volume heterogeneities in near-surface media.

Discussion and Conculsion

Rugged topographies and strong volume heterogeneities in near-surface sediments significantly affect seismic data recorded at the free surface, causing extremely low signal-to-noise ratios by semirandom scattering noises, which complicate in-site amplification behavior and hinder near-surface imaging. It is difficult to quantitatively assess near-surface seismological complexity from observed seismic data, simulated wavefields, or mathematical descriptions of near-surface geometries. In this study, the boundary–volume element numerical method was used to discretize the GLSIE formulated in terms of volume scattering and boundary scattering. The integral equation technique provided sufficient accuracy to model complex near-surface media by geometrically accurate description of rugged topographies, the explicit use of boundary conditions, and the ability to deal with volume heterogeneities. The resultant global coefficient matrix can be regarded as the combination of near-surface geometries, near-surface heterogeneities, and near-surface wavefields.

As a tentative attempt to characterize the global coefficient matrix, the ratio of the summation of all matrix elements and dimensions, to become the characteristic index as an evaluation criterion to quantitatively analyze near-surface seismological complexity, was defined. This efficient method was validated by numerous examples, whereby the resultant matrix characteristic index varied consistently with near-surface complexity in geometric structures, volume heterogeneities, and computational frequencies. The results, consistent with the previous studies in ground-motion amplification, demonstrate that as a preliminary evaluation method, the method is valid and flexible. This method can be regarded as a simple but fast technique for near-surface complexity assessment.

The main conclusions are summarized as follows.

1. The matrix characteristic index closely depends on the Green's function. The resultant H, G, and K matrices can all reflect near-surface seismological complexity in some respects.
2. The G matrix (i.e., the fundamental solution) characterizes the effect on wavefields associated with propagation distances between arbitrary boundary elements, whereas the K matrix features the volume scattering by near-surface heterogeneities.
3. The H matrix (i.e., the normal derivative of the fundamental solution) contains the information of topographic roughness in terms of the relative positions of two boundary elements.
4. As for the boundary scattering effect, the characteristic index of the H matrix is larger than that of the G matrix. This implies that the boundary roughness dominates the boundary scattering effect, which seems to conform to common sense.

Data and Resources

No data were used in this article. All plots were made using MATLAB, v.R2016a (The MathWorks, Inc., https://www.mathworks.com/products/matlab.html, last accessed September 2016).

Acknowledgments

References

Bouchon, M. (1973). Effect of topography on surface motion, *Bull. Seismol. Soc. Am.* **63,** 615–632.

Bouchon, M., M. Campillo, and S. Gaffet (1989). A boundary integral equation-discrete wavenumber representation method to study wave propagation in multilayered media having irregular interfaces, *Geophysics* **54,** 1134–1140.

Bouchon, M., C. A. Schultz, and M. N. Toksöz (1996). Effect of three dimensional topography on seismic motion, *J. Geophys. Res.* **101,** 5835–5846.

Chen, X. F. (1990). Seismogram synthesis for multilayered media with irregular interfaces by global generalized reflection/transmission matrices method, I. Theory of two-dimensional SH case, *Bull. Seismol. Soc. Am.* **80,** 1696–1724.

Fu, L. Y. (2002). Seismogram synthesis for piecewise heterogeneous media, *Geophys. J. Int.* **150,** 800–808.

Fu, L. Y. (2003). Numerical study of generalized Lipmann–Schwinger integral equation including surface topography, *Geophysics* **68,** 665–671.

Fu, L. Y. (2005). Rough surface scattering: Comparison of various approximation theories for 2D *SH* waves, *Bull. Seismol. Soc. Am.* **95,** 646–663.

Fu, L. Y., and M. Bouchon (2004). Discrete wavenumber solutions to numerical wave propagation in piecewise heterogeneous media—I. Theory of two-dimensional *SH* case, *Geophys. J. Int.* **157,** 481–498.

Fu, L. Y., R. S. Wu, and M. Campillo (2002). Energy partition and attenuation of regional phases by random free surface, *Bull. Seismol. Soc. Am.* **92,** 1992–2007.

Hu, S. Z., L. Y. Fu, and Z. X. Yao (2009). Comparison of various approximation theories for randomly rough surface scattering, *Wave Motion* **46,** 281–292.

Hudson, J. A., R. F. Humphryes, I. M. Mason, and V. K. Kembhavi (1973). The scattering of longitudinal elastic waves at a rough free surface, *J. Phys. Appl. Phys.* **6,** 2174–2186.

Sabina, F. J., and J. R. Willis (1975). Scattering of SH waves by a rough half-space of arbitrary slope, *Geophys. J. Roy. Astron. Soc.* **42,** 685–703.

Sánchez-Sesma, F. J., and M. Campillo (1991). Diffraction of *P*, *SV* and Rayleigh waves by topographic features: A boundary integral formulation, *Bull. Seismol. Soc. Am.* **81,** 2234–2253.

Sánchez-Sesma, F. J., and M. Campillo (1993). Topographic effects for incident *P*, *SV* and Rayleigh waves, *Tectonophysics* **218,** 113–125.

The State Key Laboratory of Ore Deposit Geochemistry
Institute of Geochemistry, Chinese Academy of Sciences
No. 99, Lincheng West Road, Guanshanhu District, Guiyang 550081
Guizhou Province, People's Republic of China
xhyous@foxmail.com
    (B.L.)

Institute of Geochemistry, Chinese Academy of Sciences
No. 99, Lincheng West Road, Guanshanhu District, Guiyang 550081
Guizhou Province, People's Republic of China
fuliyun@mail.gyig.ac.cn
    (L.-Y.F.)

Beijing Chinese Language and Culture College
No. 69, Qibei Street, Changping District
Beijing 102206, People's Republic of China
y_g_xin@126.com
    (G.-X.Y.)

Key Laboratory of the Earth's Deep Interior
Institute of Geology and Geophysics, Chinese Academy of Sciences
No. 19, Beitucheng Western Road, Chaoyang District
Beijing 100029, People's Republic of China
hncschengaoxiang@126.com
    (G.-X.C.)